Nanoscale

ROYAL SOCIETY OF CHEMISTRY

PAPER

View Article Online
View Journal

Check for updates

Cite this: DOI: 10.1039/d5nr05348j

Crossing the paths: the possible role of Co-based materials from lithium-ion battery recycling in the efficient electrocatalytic hydrogen production

Eleonora Carena, [a] Leire Caizán-Juanarena, [b] Andrea Marchionni, [c] Jonathan Filippi,[c] Enrico Berretti,[c] Andrea Giacomo Marrani, [d] Carlo Santoro, [a] Mohsin Muhyuddin[a] and Chiara Ferrara *[a,e]

Received 18th December 2025,
Accepted 6th April 2026

DOI: 10.1039/d5nr05348j

rsc.li/nanoscale

Cobalt is worldwide recognized as a critical and strategic raw material due to its relevance in the rechargeable battery economy, combined with limited geological availability and uneven distribution. Cobalt is also emerging for the production of electrocatalysts for hydrogen production, thus entering also in the hydrogen economy. These two are the leading technologies in the energy storage and production sector, and are expected to grow even further in the mid term future. The mindful and optimized use of critical raw materials is thus pivotal, as it is urgent to combine the high technological performance (directly associated with the use of such materials) with their adequate supply, acceptable cost, environmental and societal sustainability. In this study, we propose a possible strategy to cross the path between the two ecosystems – rechargeable batteries and hydrogen economy – for the valorization of Co derived from the recycling of spent lithium-ion batteries in the production of electrocatalysts. The materials derived from the two main recycling strategies are fully characterized in terms of Co and carbon content, structure, and morphology, and subsequently electrochemically tested under half cell conditions in alkaline media for oxygen reduction reaction, oxygen evolution reaction and hydrogen evolution reaction, demonstrating the feasibility of valorization.

Introduction

Rechargeable batteries and the hydrogen economy (production and use of hydrogen) are the leading technologies driving the shift from fossil fuels to electrification of energy production and storage.[1] Alongside the several benefits from these two major technologies (clean energy storage and production, high efficiencies, scalability, and reusability), some specific challenges still affect both technologies. Indeed, lithium-ion batteries (LIBs), water electrolyzers (WEs), and fuel cells (FCs) today on the market provide high and relevant electrochemical performance, granted by the presence of electrochemically active materials with high content of critical raw materials (CRMs) such as Li, Co, Ni, Mn, graphite, Pt, Ir.

CRMs are so defined on the basis of their scarcity, poor sustainability in the extraction process, uneven geological distribution, and high market demand. The definition of CRMs, but most importantly their use, supply, and recycling, is nowadays worldwide constrained by several regulations, recognizing their strategic role in the energy economy.[2–6]

Focusing on LIBs, the cathode materials are those reporting the highest content of CRMs, as the most diffuse on the market are $LiCoO_2$, $Li(Ni/Co/Mn)O_2$, $Li(Ni/Co/Al)O_2$, $LiMn_2O_4$, and $LiFePO_4$.[1,7,8] For this reason, recycling strategies and research are focused on the cathode. Several classes of approaches have been reported and explored, including pyrometallurgy,[7,9–11] hydrometallurgy,[10,12,13] and solvometallurgy.[14–17] Globally, two main strategies can be recognized behind these methods: the recovery of CRMs and the direct recycling. The former is based on the degradation of the cathode materials to recover Co and Ni (primary focus on today's industrial procedure) in the form of oxide or salt, with sufficient purity to be reused (mainly in the LIBs value chain), and it is the main strategy at the base of pyro- and hydro-metallurgical approaches. The latter is a more recent working scheme, which emerged from the idea of closing the loop of

---

[a] Department of Materials Science University of Milano-Bicocca, U5, Via Roberto Cozzi 55, 20125 Milan (MI), Italy. E-mail: chiara.ferrara@unimib.it
[b] Departmento de Física Aplicada I, Facultad de Ciencias, Universidad de Málaga, Málaga, 29071, Spain
[c] Institute of Chemistry of Organometallic Compounds (ICCOM) National Research Council (CNR), Via Madonna del Piano 10, Sesto Fiorentino, 50019, Italy
[d] Department of Chemistry, "Sapienza" University of Rome, P.le Aldo Moro 5, I-00185 Rome, Italy
[e] National Reference Center for Electrochemical Energy Storage (GISEL), Consorzio Interuniversitario Nazionale per la Scienza e Tecnologia dei Materiali (INSTM), via Giusti 9, 50121-Firenze, Italy

the circular economy scheme: as the CRMs derived from recycling of LIBs are often reused for the production of new cathodic materials, the trend is to degrade cathodic materials, avoid the separation step of CRMs, and directly resynthesize new cathodes.[18] This idea is implementable mainly starting from hydro- and solvo-metallurgical approaches.[18–20] The production of the so called "battery grade" cathode material (*i.e.* materials with sufficient purity and structural/morphological characteristics making them suitable for implementation in LIBs and ensuring high performance) represents a challenge, and at each step of cell manufacturing, the generation of scrap is still very high, increasing the production cost and posing the question of materials recycling and/or reuse.[21,22]

In parallel, the hydrogen economy relies very much on CRMs.[23–30] Ideally, a large fraction of hydrogen will be produced using WEs, which use renewable energy, making the process green and sustainable.[31,32] WEs' technology is somewhat mature, but some critical points have to be overcome before large-scale commercialization. Hydrogen can be used as fuel in FCs, where the chemical energy is transformed into electricity without emission of greenhouse gases, closing the circle of production and usage of hydrogen in a sustainable way.[33,34]

Proton exchange membrane (PEM) technologies, in particular, are the most efficient ones, but they are strictly dependent on the usage of CRMs as electrocatalysts.[35–37] In PEM fuel cells (PEMFCs), platinum supported over carbon (Pt/C) is strongly used as both anode and cathode electrocatalyst.[38,39] The loading on the cathode is higher due to the sluggish oxygen reduction reaction (ORR).[40,41] In PEM water electrolyzers (PEM-WEs), iridium oxide is used on the anode electrode and platinum supported over carbon (Pt/C) on the cathode electrode.[42–44] Both Pt and Ir are rare, scarce and very expensive; this, in turn, increases the capital cost of the WEs, limiting their wide commercialization. Moreover, at the moment, there is no established recycling chain in place to recover and reuse platinum group metals (PGMs) or CRMs.[45,46]

In parallel, alkaline technology relying on a liquid alkaline supporting solution and an anion exchange membrane (AEM) is gaining momentum and interest.[47,48] In fact, despite still being inferior compared to PEM technology, alkaline and AEM technologies can operate without PGMs on both anode and cathode.[23,49] Considering fuel cells, alkaline fuel cells (AFCs) are not as efficient as a liquid electrolyte separates the anode and cathode electrodes, which are positioned at a high distance (millimetre scale) and therefore they have high ohmic resistance and low power density output.[50,51] The introduction of a solid polymeric AEM for fuel cell (AEM-FC) has critically advanced this technology, making it comparable to PEM-FCs.[52,53] In AEM-FC, the anode is based on Pt/C but the loading is low and it does not affect the overall cost.[54] On the contrary, due to the sluggish ORR, Pt/C loading on the cathode is generally one order of magnitude higher compared to the anode. In AEM-FC, Pt/C has been successfully replaced using atomically dispersed transition metals (TMs) coordinated with nitrogen on a carbon backbone (TM-N_x-C) with TMs as Fe, Mn, Ni, Co, *etc.*[55–59] but also by TMs oxides capable of both acting as intermediate scavengers and electrocatalytic active sites for ORR in an alkaline environment.[60–63]

Concerning AEM-WE technologies, they seem to be more promising compared to alkaline WE, as the usage of the solid polymeric membrane helps the separation of gases and their pressurization compared to alkaline WE. In AEM-WE, the most promising anode electrocatalyst where oxygen evolution reaction (OER) occurs, relies on Ni_x–$Fe_{(1-x)}OOH$, which in an alkaline environment is stable, durable, and has high electrocatalytic activity[64–67] Other TMs and their oxides have also been investigated.[48] At the cathode side, where hydrogen is developed during the hydrogen evolution reaction (HER), nickel-based electrocatalysts supported over carbon seem to be promising.[48] In a recent comprehensive review, various TMs (Ni, Mo, Fe, Co, *etc.*) as metallic nanoparticles, alloys, oxides (single and mixed), supported over carbon matrices were studied with promising results.[68,69]

Based on these scenarios, in the present study, we propose the valorization of products and scraps derived from LIB's recycling paths and exploit them for reactions of interest taking place at the electrodes of AEM-FCs and AEM-WEs. ORR is a bottleneck taking place at the cathode side of AEM-FCs, while HER and OER are both limiting reactions, taking place at the cathode and anode of AEM-WE, respectively.[63,70] The strategies and procedures for LIBs' cathode recycling have been previously investigated by our group, exploring both the possibility to recover CRMs for their subsequent use[16] and the possibility to directly resynthesize the cathode material.[71] The products obtained from these recycling paths are considered for other relevant applications.

Indeed, in this manuscript, two recovery strategies and upcycling routes have been investigated. An initial recovery route considered was the principal industrial route that con-

Chiara Ferrara

Chiara Ferrara is Associate Professor at the Department of Materials Science at the University of Milano-Bicocca since 2025. She holds a joint Ph. D. in Chemistry from the University of Pavia and ENS de Lyon, specializing in solid-state NMR. Her research focuses on the design and structural investigation of materials for lithium- and sodium-ion batteries, utilizing advanced diffraction techniques to fill the gap in correlation of structural features with functional properties. Currently, her interests reach also the development of innovative methods for lithium-ion battery recycling and the recovery of critical raw materials; she coordinated different academic and industrial research projects.

sists of the recovery of cobalt, with its separation from the waste cathode components. The second strategy instead intends to resynthesize the cathode material directly without separation. The products of both recovery strategies containing Co as the main TM of interest were mixed with high surface area carbon black and tested as PGM-free electrocatalysts for ORR, OER and HER in alkaline media to highlight their potential application in these specific reactions to replace expensive critical materials.

Experimental

Materials preparation

The idea behind the selection of materials is presented in Fig. 1.

The initial black mass has been recovered from spent smartphone batteries disassembled after discharge (by immersion in a saline solution for two days and drying overnight). They were manually dismantled to recover the cathode side, from where the powder was carefully scratched from the current collector. The final powder sample is labelled “Black Mass” in the following and has been characterized by XRD, XPS, XRF, SEM, TEM, EDX and ICP-OES analysis prior to the following use.

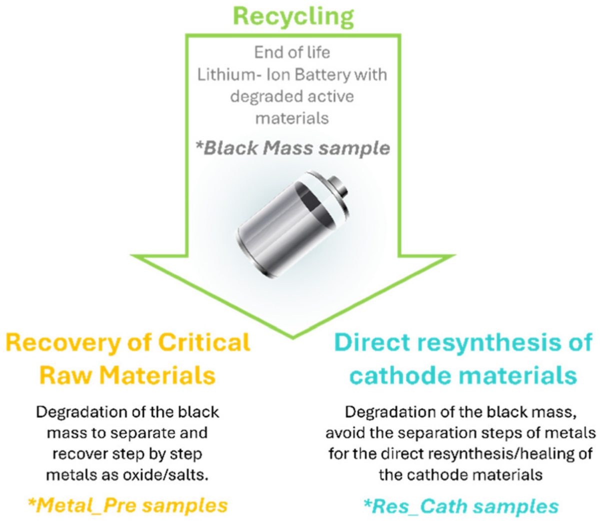

Fig. 1 Recycling of LIBs: a sketch of the two main strategies outlined from literature analysis and the positioning of the samples considered in the present paper within the LIBs value chain.

The black mass has been subjected to two distinct processes. With the first one, the black mass is degraded through a solvometallurgical approach using choline citrate, ethylene glycol, and citric acid as a deep eutectic solvent (DES). The obtained product is then thermally treated to obtain a solid mass that can be washed (water leaching) to recover Li in solution as LiCl. The remaining solid is further thermally treated to obtain metal oxides, as previously described; this thermal treatment is explored in the range of 300°–500 °C.[16] An intermediate product is thus obtained, the precursor of the metal oxides with a high content of carbon fraction, highly dependent on the temperature of the heating treatment, is here exploited and tested for the formulation of electrocatalysis, hereafter labelled as “Metals_Pre_*X*” in the following, with *X* indicating the temperature of the thermal treatment.

With the second process, the black mass is degraded through the use of a different DES, based on a mixture of choline citrate–ethylene glycol. In this case, it is possible to directly resynthesize the cathode material at the end of the recycling procedure; the temperature of the heating treatment can be varied in the 550°–850 °C temperature range. The samples derived from this procedure are labelled “Res_Cath_*X*” in the following, where *X* indicates the temperature reached during the resynthesis.[71] The full list of samples, together with sample labelling and experimental conditions for their obtaining is reported in Table 1 for convenience.

Investigation

XRD data have been collected with the use of a Rigaku Miniflex 600 powder diffractometer (Cu Kα radiation), in an angular range 5°–80°, 0.2 step size, 10 deg $\min^{-1}$. Inductively Coupled Plasma-Optical Emission Spectroscopy data have been collected using a ICP-OES, Thermo Scientific CAP7400Duo instrument, equipped with a quartz torch, a charge injection detector and a CetacASX-560 autosampler. Samples have been obtained by dissolving the solid materials in an acidic aqueous matrix, with a calibration curve based on 5 standard solutions from 5 ppm to 30 ppm. Carbon content has been estimated through elemental analysis with PerkinElmer PE2400-Series II, CHNS/O analyzer. Energy-dis-

Table 1 Samples considered in the present paper together with the experimental conditions considered for their preparation

Sample	Origin	Treatment	Expected composition	Ref.
Black mass	Recovered from spent LIBs	Mechanical disassembly	$LiCoO_2$ active material, carbon, polymeric binder	—
Metal_Pre_300 Metal_Pre_400 Metal_Pre_500	Solvometallurgical treatment of the black mass sample	Choline chloride–ethylene glycol based full dissolution. The so-obtained product has been dried and undergone a thermal treatment at 300°, 400°, and 500° C, respectively.	Co oxides, carbon	16
Res_Cath_550 Res_Cath_650 Res_Cath_750 Res_Cath_850	Solvometallurgical treatment of the black mass sample	Choline citrate–ethylene glycol based full dissolution. The so-obtained product has been exploited for direct resynthesis with final thermal treatment at 550°, 650, 750°, and 850 °C, respectively.	$LiCoO_2$	71

persive X-ray fluorescence (XRF) qualitative analysis was performed using a Bruker Artax 200 spectrometer with a Mo anode X-ray tube. For XPS characterization the powder samples were spread onto In foils attached to the sample holder with conductive scotch tape. XPS measurements were performed using an Omicron NanoTechnology Multiprobe MXPS system equipped with a monochromatic X-ray anode (Omicron XM-1000) and an achromatic dual X-ray anode (Scienta Omicron DSX 400). The experimental conditions adopted were the following: excitation by Al Kα photons ($h\nu$ = 1486.7 eV, monochromatic X-ray radiation) and Mg Kα photons ($h\nu$ = 1253.6 eV, achromatic X-ray radiation), both generated operating the anode at 14 kV, 16 mA, and a take-off angle of 21° with respect to the sample surface normal. All narrow-range photoionization regions were recorded with a 20 eV pass energy, while the survey spectra with 50 eV pass energy. The binding energy (BE) of the C 1s line at 284.8 eV, associated to adventitious carbon species, was used as an internal standard reference for BE scale (accuracy of ±0.1 eV). The achromatic Mg Kα source was used taking advantage of its high intensity and low electrostatic charge-inducing capability during measurement. On the other hand, the monochromatic Al Kα source allowed for a better resolution, but suffered from a lower S/N ratio and a higher charging effect on the sample.

The Co 2p experimental spectra were theoretically reconstructed by fitting the secondary electrons background to a Shirley function and the elastic peaks to symmetric pseudo-Voigt functions described by a common set of parameters (position, FWHM, Gaussian–Lorentzian ratio) free to vary within narrow limits. The Gaussian–Lorentzian ratio varied between 0.8 and 0.9. Experimentally determined area ratios (with 10% associated error) were used to estimate XPS atomic ratios between relevant element components, after normalization for the corresponding photoionization cross sections according to Scofield calculations[72] and for the square root of photoelectron kinetic energy.

Morphological analysis has been performed with a Zeiss Gemini 500 on samples previously metallized with Au : Pd 70 : 30. TEM, STEM and EDS-STEM data of the samples have been acquired using a Thermo Fisher Talos F200X microscope. Image acquisition and EDS were collected using a beam energy of 200 kV. For the characterization, small amounts of sample powder were sonicated for fifteen minutes in isopropanol. The obtained mixture was drop-cast onto Cu holey TEM grids, and let dry.

Electrochemistry

The derived materials were first mixed with commercially available carbon black, particularly Ketjenblack EC-600JD (KJB, Nanografi), in a ratio of 50 : 50. The mixing was done using a mortar for 30 minutes, until a uniform blend of the electrocatalyst was obtained, which was afterwards used to configure the working electrode. Subsequently, an electrochemical ink was produced by mixing 5 mg of the aforementioned powder blend in a solution containing 985 µl of isopropanol (Alfa Aesar) and 15 µL of Nafion® D-520 (5 wt%, Alfa Aesar). The inks were probe sonicated for 30 minutes to achieve a homogeneous consistency with a very good suspension. Using a Pine WaveVortex rotating disk electrode (RDE) assembly connected with a Pine bipotentiostat, electrochemical analyses were carried out in a typical three-electrode configuration. The reference electrode was Ag/AgCl, whereas a graphite rod worked as a counter electrode. For HER and OER, the working electrode was configured by drop casting the electrochemical ink equivalent to 0.6 mg cm^{-2} mass loading on the glassy carbon disk (having a geometric area of 0.1963 cm^2) of RDE (E5 series) using a precision pipette and dried at room temperature. Similarly, for ORR measurements, the working electrode was configured by depositing the same 0.6 mg cm^{-2} mass loading on the glassy carbon disk (0.2376 cm^2) of the rotating ring disk electrode (RRDE, E6R2 series). The HER and ORR measurements were carried out in N_2-saturated 1 M KOH (pH 14), while the ORR measurements were recorded in O_2-saturated 0.1 M KOH (pH 13). All the electrochemical measurements were recorded under hydrodynamic conditions while maintaining the RDE or RRDE rotation speed at 1600 rpm. In this work, all the potential values are presented on a reversible hydrogen electrode (RHE) scale by adding the factor of $E_{\mathrm{Ag/AgCl}}$ + 0.0591pH to the measured potential, where $E_{\mathrm{Ag/AgCl}}$ was 0.197 V. For each analysis, *i.e.*, HER, OER and ORR, linear sweep voltammograms (LSVs) were acquired in the respective potential windows at the scan rate of 5 mV s^{-1} after running multiple cyclic voltammetries to achieve a steady trend in the current values.

During the ORR measurements, the potential of the Pt ring of RRDE was fixed at 1.2 V. By monitoring the disk current (I_{disk}) and ring current (I_{disk}), peroxide yield (%) and number of electrons during ORR (n) were estimated according to eqn (1) and (2), respectively, where N is the collection efficiency (38%) of the RRDE.

$$\text{Peroxide }(\%) = (200I_{\mathrm{ring}}/N)/(I_{\mathrm{disk}} + I_{\mathrm{ring}}/N) \qquad (1)$$

$$n = 4I_{\mathrm{disk}}/(I_{\mathrm{disk}} + I_{\mathrm{ring}}/N) \qquad (2)$$

Note that the ORR electrochemical data are presented after manual background subtraction.

Results and discussion

The materials used for the preparation of the electrocatalysts have been characterized in terms of composition, structure, and carbon content. The XRD analysis is reported in Fig. 2a and reveals that the black mass sample is composed of a layered cathode compatible with $LiCoO_2$ (LCO) and/or $Li(Ni/Co/Mn)O_2$ (NMC) systems (ref. card 98-018-2442, the LCO and NMC present the same crystallographic structure and very similar cell parameters), a fraction of deeply delithiated LCO and/or NMC phase (reference 98-017-2912), and a fraction of Co_3O_4 (98-006-9375), not surprisingly considering material is coming from disposed LIBs. The black mass sample has been further characterized to determine the chemistry of the

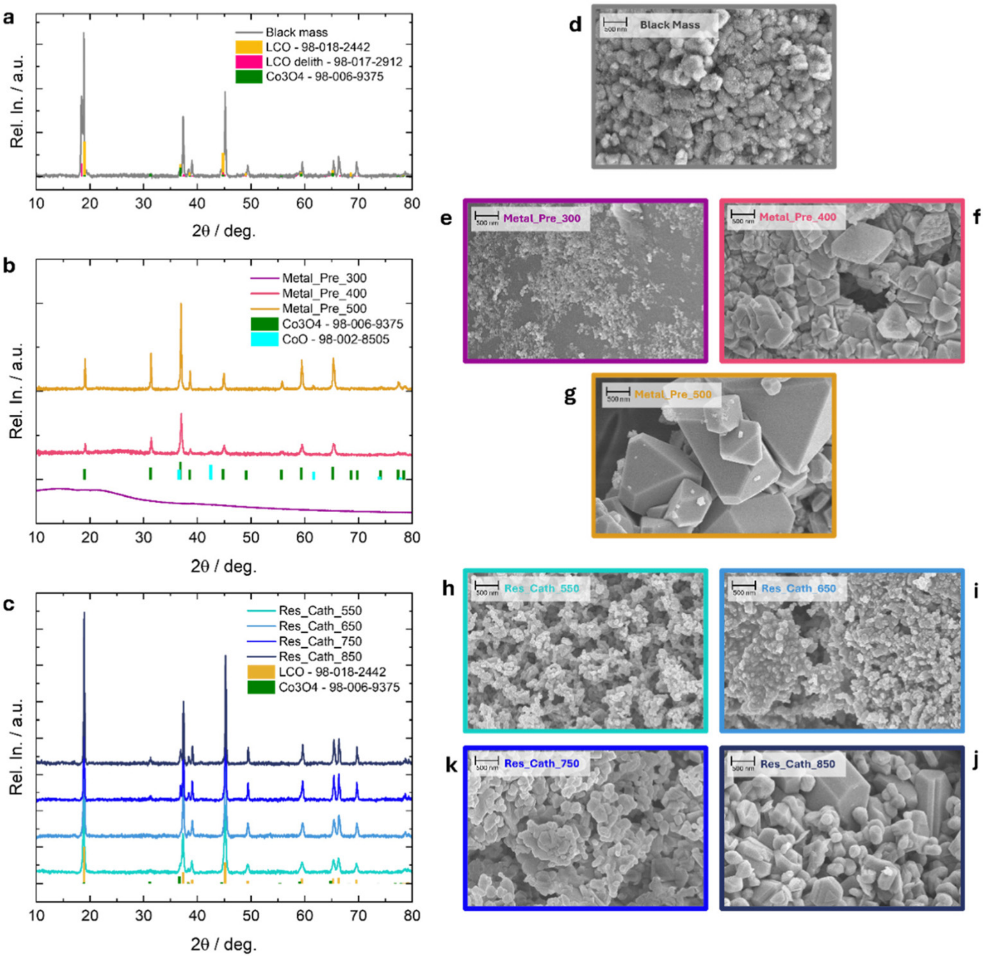

Fig. 2 XRD patterns obtained for the black mass (a), Metal-Pre series (b), and Res_Cath series (c) samples together with the reference compounds ($LiCoO_2$ card 98-018-2442 and partially delithiated $Li_{0.35}CoO_2$ card 98-017-2912, cobalt oxides *i.e.* Co_3O_4 card 98-006-9375, CoO card 98-002-8505) and corresponding SEM images (d–j).

cathode: the elemental composition has been explored through XRF, CHNS, and ICP analysis, and full information can be found in Table S1 and Fig. S1. The sample presents Li and Co with a ratio different from the one expected by the $LiCoO_2$ pristine compound (0.67 : 1 Li : Co), compatible with the degraded state of the battery. Carbon is also present, but in a small amount. Overall, these results confirm that the black mass is derived from spent LIBs based mainly on LCO cathode material; the carbon content is associated with the formulation of the electrode, generally involving the presence of 3–8% of conductive carbon and polymeric binder. The morphology of the sample (Fig. 2d) demonstrates a large distribution of particle size; moreover, the EDX maps (Fig. S3a) further confirm the dominant contribution of Co. Other elements (Mn, Ni, F, P) are revealed in very low amounts (0.5 at%) and are again compatible with traces from the cell components (electrolyte residues, binder).

The series Metal_Pre presents a strong evolution of the phase composition with the temperature as evident from the XRD data reported in Fig. 2b. We recall here that the whole Metal_Pre series is derived from a step of a solvometallurgical process that aims to recover separately Co and Li.[16] Co is obtained after the water leaching of the soluble Li fraction; Co is retained in the carbonaceous matrix and subsequently converted into crystalline oxide with intermediate temperature treatments.[16] Based on this, it is straightforward to rationalize the data obtained for this series. The sample treated at 300 °C appears as amorphous, and from the compositional point of view, the carbon content is extremely high (about 70% as from Table S1). Cobalt is the only metal present, as detected from XRF and ICP analysis. ICP also excludes the presence of lithium, demonstrating the efficiency of the separation process. The sample is composed of small particles, in the 20–50 nm range with almost spherical shape (see Fig. 2e and Fig. S3b). Both the phase composition and the morphology changes moving to the Metal_Pre_400: in the corresponding XRD pattern, some reflections appear on the background, still strongly modulated. The reflections are compatible with the Co_3O_4 and CoO phases (ref. 98-006-9375 and ref. 98-002-8505); their broadening suggests these species are not fully crystalline and/or have small diffraction domains. The carbon content is decreased with respect to the Metal_Pre_300 case, but is still very high (~50%). The particles present a wide distribution in shape and dimensions, with agglomerates of small primary particles together with large, well-formed crystals with pointed shape (1 μm), characteristic of spinel structures. Finally, for the Metal_Pre_500, the carbon content is strongly diminished (~13%), the crystal phases revealed by the XRD analysis are Co_3O_4 and CoO with higher crystallinity, as also confirmed by the more ordered morphology and larger particles, with highly ordered micrometric crystals. In this series of samples, the composition changes significantly as the carbon content is very high and variable (10–70%), while the Co is found as oxide with different degrees of crystallization.

Differently, the series Res_Cath is obtained from the resynthesis step of a solvometallurgical process for the recycling of LIBs.[71] Co and Li are expected to be present, while the carbon content should be very low. These considerations are confirmed by the phase and compositional analysis reported in Table 2. The XRD of the whole series (Fig. 2c) evidences the presence of LCO as the dominant crystalline phase; nevertheless, Co_3O_4 is always present as a secondary fraction, as evident from main reflections at 32 and 37 deg. The carbon content is very low (<1%), but the presence of cobalt oxide impurities make these samples not compatible with the electrochemical grade and standards required for battery application, classifying these batches as production scraps. The carbon content is negligible, as expected from the synthesis procedure and thermal history of the sample, while the Li and Co ratio is quite low, in the range of Li : Co 0.7–0.9 : 1 (under-stoichiometry of Li). This is compatible with the presence of Co_3O_4 as a secondary phase. Overall, this confirms the low quality of these resynthesis batches that can thus be classified as production scrap not meeting the standards for the application in LIBs.

Beside the characterization of the bulk materials, the surface chemistry has been characterized through implementation of XPS analysis (Fig. 3) and morphological investigation (Fig. 4), as it represents the key aspect in determining the final electrocatalytic performance. The raw XPS spectra in the Co 2p

Table 2 Compositional analysis for all the samples considered in the present study. Carbon content from CHNS, Li and Co quantification from ICP analysis, and other eventual metal traces from XRF, EDX analysis

Sample	C/w%	Co/molar%	Li/molar%	Other elements/<1%
Black mass	2.61	1	0.73	Mn, Ni, F, P, Si, Cu, Al
Metal_Pre_300	69.00	1	—	Cl
Metal_Pre_400	53.54	1	—	Cl
Metal_Pre_500	13.73	1	—	Cl
Res_Cath_550	0.19	1	0.74	Zr, Si, Fe
Res_Cath_650	0.09	1	0.73	Zr, Si, Fe
Res_Cath_750	0.09	1	0.81	Zr, Si, Fe
Res_Cath_850	0.04	1	0.90	Zr, Si, Fe

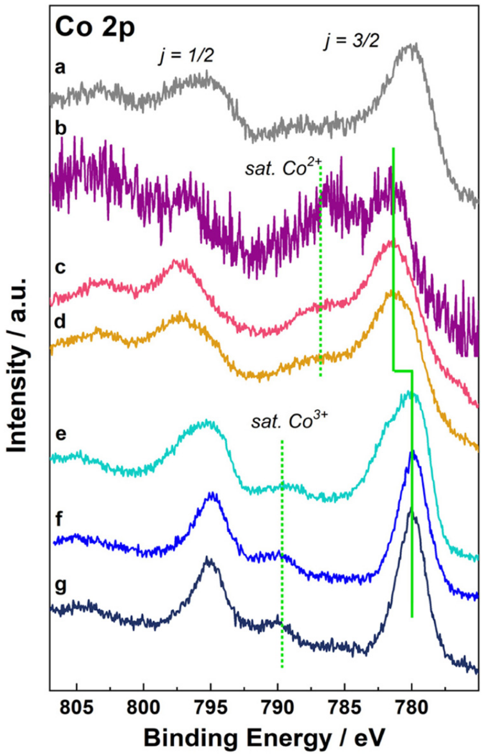

Fig. 3 Co 2p XPS spectra recorded with Mg Kα radiation of (a) black mass; (b) Metal_Pre_300; (c) Metal_Pre_400; (d) Metal_Pre_500; (e) Res_Cath_550; (f) Res_Cath_750; (g) Res_Cath_850.

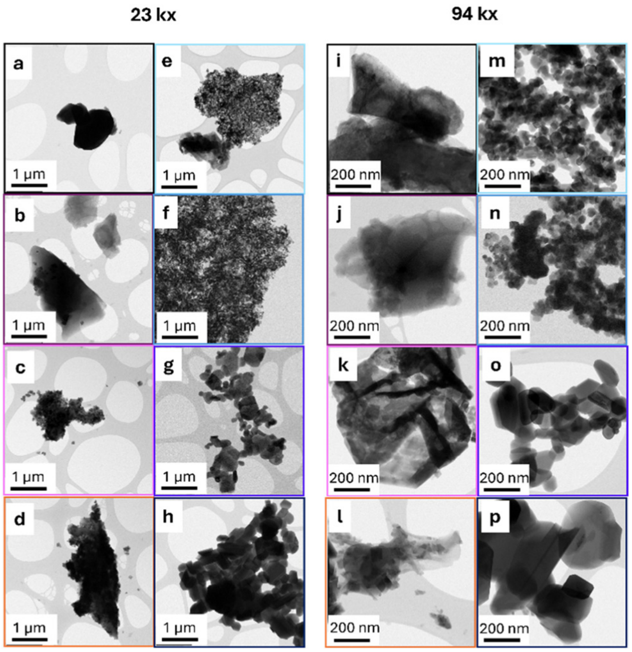

Fig. 4 STEM Bright field images for all the samples presented in the study at two different magnifications: 23kx (first two columns) and 94kx (last two columns). (a) and (i) represent the black mass, (b) to (d) and (j) to (l) represent Metal_Pre_300, 400 and 500 respectively, while (e) to (h) and (m) to (p) represent Res_Cath_550, 650, 750 and 850.

photoionization region recorded with the intense Mg Kα source are reported in Fig. 3, allowing for a straightforward comparison of all samples. All spectra show the Co 2p spin–orbit doublet with the low-BE $j = 3/2$ and high-BE $j = \frac{1}{2}$ portions separated by an energy of 15 eV (ΔE_{SO}). In all the samples of the Metal_Pre series (Fig. 3b–d), an intense contribution in the $2p_{3/2}$ part at 781.5 eV can be seen, followed by a broader and less intense feature around 787 eV. The resulting lineshape is similar to the one previously reported for CoO, where Co^{2+} centers are coordinated by O^{2-} anions in an octahedral environment, resulting in a high-spin (HS) $t_{2g}{}^5$ $e_g{}^2$ configuration.[73–76] Curve-fitting deconvolution of the high-resolution (Al Kα) Co 2p spectrum of the Metal_Pre_500 sample (Fig. S2 and Table S2) shows a satisfactory match with the known final state multiplet reported for highly correlated Co compounds. In fact, the $2p_{3/2}$ portion of the spectrum was fit to 3 components associated with the two charge-transfer final states ($2p^{-1}3d^8L^{-1}$ and $2p^{-1}3d^9L^{-2}$, low BE) and the high-BE unscreened $2p^{-1}3d^7$ state, commonly reported as a satellite.[73,76,77] Turning to the Co 2p spectra of the Res_Cath series (Fig. 3e–h) they all appear very similar except for a probable charge-induced broadening in the Res_Cath_750 sample. In the Res_Cath samples the lineshape is different from the Metal_Pre series, with a main $2p_{3/2}$ component falling at 780.0 eV and an apparent satellite around 790 eV. The position and the shape of the spectral features is compatible with the literature data on $LiCoO_2$ (LCO), where the Co^{3+} contribution is expected to be predominant.[77–80] Indeed, curve-fitting of the high resolution spectrum of Res_Cath_650 sample (Fig. S2 and Table S2) enabled deconvolution of experimental data using the reported doublet (red curves) for the low-spin (LS) octahedral Co^{3+} ions ($t_{2g}{}^6$), which includes the charge-transfer final state ($2p^{-1}3d^7L^{-1}$ at 779.9 eV) and the unscreened (satellite) final state ($2p^{-1}3d^6$ at 789.9 eV).[77,81,82] Furthermore, some weaker additional components (blue curves) were required to account for residual intensity in the 781–787 eV range. According to the literature, a satisfactory curve-fitting was achieved using contributions from tetrahedral HS Co^{2+} ions ($e^4t_2{}^3$) in the $2p^{-1}3d^8L^{-1}$, $2p^{-1}3d^9L^{-2}$, and $2p^{-1}3d^7$ final states at increasing BE.[81–83] It is to be noted that a mixed Co^{3+}/Co^{2+} composition is also compatible with the trace presence of the Co_3O_4 spinel. Finally, the black mass sample (Fig. 3a) displays a Co 2p lineshape rather similar to the one in Res_Cath series, though with slightly broader features and a less defined satellite, which point at the presence of $LiCoO_2$ with a probable more significant contribution from Co_3O_4. Globally, the XPS analysis reveals that the Metal_Pre series is compatible with the presence of CoO, though due to the broad signals recorded, a contribution from Co_3O_4cannot be ruled out; the Res-Cath series shows the presence of $LiCoO_2$ as a major component and a minor fraction of Co_3O_4. Along the two series, the effect of heat treatment temperature can hardly be discerned. Overall, the XPS conclusions are in line with the results obtained from XRD, showing a negligible evolution of the phase and surface composition with the temperature reached during the preparation, while the two series are different in terms of phases: Co oxides for the Metal-Pre series, and $LiCoO_2$ for the Res-Cath series. Finally, it must be considered that the species determined in the pristine powders are considered as the starting configuration of the electrodes and are expected to possibly evolve under the working conditions (*i.e.* under alkaline media exposure).[83,84] This eventual surface evolution is highly beneficial as the surface recontruction leads to the formation of the active sites, involving phenomena related to amorphization and/or formation of Co defective surface species, including oxides and hydroxides.[84,85]

The morphology of the powders changes with the temperature explored in the preparation: indeed, the particles obtained at low temperature are spherical and in the range of 100 nm, while their dimension and shape evolve up to the formation of pointed micrometric particles with the highest temperature reached in the resynthesis. Overall, to summarize the results for this series, the dominant compound is $LiCoO_2$ with no carbon residue and a significant variability in the morphology.

The morphology and elemental distributions have been characterized further as they have deep impact on the final electrocatalytic properties; the STEM images are reported in Fig. 4, and coupled with EDX maps in Fig. S3. For the black mass, morphological analysis shows almost-spherical particles with dimensions which span from 500 nm to 2 mm. The particles show a bimodal order: (i) a sintered-like structure, with smaller entities which adhere to form the bigger objects and (ii) a dense structure which shows no hollowness. These two structures appear to be present simultaneously in the powder. A similar discontinuous structure can be seen for the Metal_Pre series, with inclusion of bigger, ordered crystals inside a discontinuous structure for the Metal_Pre_500. Finally, for the Res_Cath series, particles on form of denser, defined crystals can be seen, with almost no presence of different structures. For this series, an important increase in crystal dimensions can be noticed following the increase in temperature. For the 550 and 650 samples, particles appear faceted, tending to spherical, with dimensions in the range 30–50 nm. An increase in temperature between 650 °C and 750 °C, and between 750 °C and 850 °C produces a ripening, which leads to an increase in dimensions of the particles, and to a loss of a defined geometric shape. EDS was used to define the chemical nature of these structures. By EDS mapping, it was possible to associate the dishomogeneous structure visible in the black mass and in the Metal_Pre samples to a carbon-rich phase. Apart from the carbon areas, all the samples showed homogeneous cobalt and oxygen distribution, with Co/O at ratio in line with the stoichiometry of the main phases expected by XRD; $LiCoO_2$ for black mass and Res_Cath, and Co_3O_4 for Metal_Pre. Chlorine is visible as a minority component (<4 wt%) in all the Metal_Pre series, while it appears as traces (<1 wt%) in the black mass. No chlorine signal was detected for the Res_Cat series. Along Cl, also P, S, Ti, and Mn were detected as trace elements (<1 wt%) in the black mass, Zr, Si and Fe for the Res_Cath and Si for the Metal_Pre. The presence of such trace elements, with particular attention for

N and Cl impurities, has already been considered and discussed. Although they can be considered as contaminants derived from the specific production routes of the samples considered in this studies, the introduction of N and Cl can actually present a benefical role. Indeed low doping level (~1–2%) has been associated with a synergistic effect, formation of edditional defects and active sites, and improved ORR activity by modulation of the electronic density of the carbonaceous matrix.[86,87]

EDS is unable to detect and quantify Li. Still, Selected Area Electron Diffraction (SAED) helped us to qualitatively confirm XRD results regarding the presence of a LCO phase. SAED highlighted the presence of both trigonal $LiCoO_2$ and cubic Co_3O_4 for the black mass sample, and exclusively $LiCoO_2$ for the Res_Cath series. For the Metal_Pre series, Co_3O_4 was the only visible phase. By the study of FFT on HR-TEM images, no fringes related to graphitic carbon were visible, suggesting its presence in the form of amorphous C.

All the samples are thus of potential interest for application in ORR, HER, OER as they present cobalt oxide in various forms (nanometric to micrometric particles, disordered and crystalline, supported on carbon or without carbon content). For this reason, all the samples have been tested as possible active materials. The results are presented for the two series of samples derived from the strategies reported in Fig. 1, *i.e.* the recovery of critical raw materials (first strategy) and the direct resynthesis of cathode materials (second strategy).

Upgrading LIB waste sample using the first strategy – recovery of CRMs

Oxygen reduction reaction electrocatalytic activity for Metal-Pre-*X* samples. The results related to the ORR in alkaline media obtained from the electrocatalysts obtained through the first valorisation route, with the formation of cobalt oxides, are reported in Fig. 5.

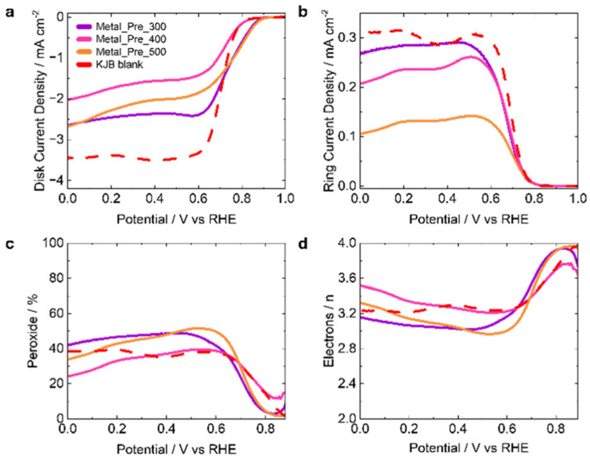

Fig. 5 Oxygen reduction reaction (ORR) performance of the samples of the Metal_Pre_*X* series supported over 50% KJB. (a) Disk current density, (b) ring current density, (c) peroxide production and (d) number of electrons exchanged.

As discussed, the three samples representing this series differ in the carbon content and crystallinity/morphology of the cobalt oxides formed during calcination. When considering onset potential (E_{on}) derived from the sigmoidal current–potential ORR curves, the values obtained are 810 mV *vs.* RHE for Metal_Pre_400, and 875 mV *vs.* RHE for Metal_Pre_500, and 865 mV *vs.* RHE for Metal_Pre_300. The half-wave potential ($E_{1/2}$) of these electrocatalysts during ORR ranges from 0.700 V *vs.* RHE (Metal_Pre_300) and 729 mV *vs.* RHE (Metal_Pre_500). The limiting current was in the range of 2.0 mA cm^{-2} and 2.6 mA cm^{-2} (Fig. 5a), which was lower compared to the theoretical value, indicating a non-complete four-electron reaction mechanism. From the ring current densities (Fig. 5b), it can be seen that as the overpotential initially increases, the ring currents shoots up and then shows a declining trend. It is noteworthy that the Pt ring surrounding the glassy carbon electrode of RRDE is used to real-time detect peroxide content produced at the disk deposited with the electrocatalyst. Therefore, the implication of ring current can be seen on the peroxide production profiles of the electrocatalysts shown in Fig. 5c. Remarkably, the peroxide produced increased at low overpotentials and decreased at high overpotentials, indicating that these electrocatalysts have the ability to reduce the peroxide intermediate at higher overpotentials. The number of electrons exchanged is reported in Fig. 5d and it varied from *ca.*3.0–3.2 at 600 mV *vs.* RHE to *ca.* 3.2–3.5 at 0 V *vs.* RHE.

Hydrogen evolution reaction and oxygen evolution reaction results for Metal-Pre-*X* samples. LSVs reporting HER and OER electrocatalytic activities of the samples prepared using the first upgrading strategy are reported in Fig. 6a and b, respectively, whereas the corresponding Tafel plots are provided in the SI as Fig. S6a and b. Also, in this case, the differences among the three electrocatalysts consisted of the temperature treatment that the samples were subject to.

Both HER and OER electrocatalytic activities were poor independently of the temperature treatment of the samples of the series Metal_Pre_*X* (*X* = 300, 400 and 500 °C). The best performing sample among the three explored was Metal_Pre_300. HER overpotentials were measured as 480 mV at −10 mA cm^{-2} (Fig. 6a) and OER overpotentials were 569 mV at 10 mA cm^{-2} (Fig. 6b). The worst performing sample was Metal_Pre_500, treated at 500 °C with HER overpotentials of 580 mV at

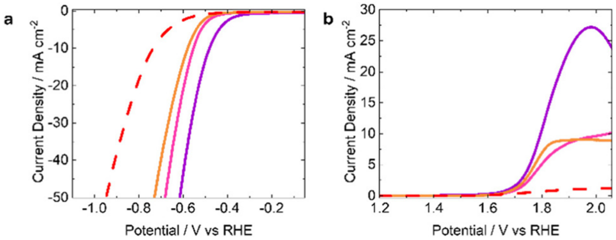

Fig. 6 (a) HER electrocatalytic activity and (b) OER electrocatalytic activity of the samples of the Metal_Pre_*X* series supported over 50% KJB.

−10 mA cm^{-2} and OER did not cross 10 mA cm^{-2} current density even at 800 mV overpotential (Fig. 6b).

These results can be rationalized considering the synergistic combination of the carbon matrix with amorphous and nanometric cobalt oxides, as evidenced by the XRD, CHNS, and TEM analysis presented in the first section. The Metal_Pre_500 sample presents a higher content of electrochemically active cobalt oxides with respect to the carbon matrix, but the larger and ordered particles are not effective in contributing to the HER and OER.

The testing of this series of samples demonstrates that their use in OER and HER is not adequate. In fact, for OER in alkaline media, an overpotential of 300 mV can be easily achieved, comparing the results obtained in literature with NiFe-based materials.[48] Similarly, the overpotentials for HER, using platinum group metal-free (PGM-free) electrocatalysts, mainly Ni/C and NiMo/C, showed an overpotential of 50–200 mV at 10 mA cm^{-2}.[48] The high production of peroxide might suggest a possible exploitation of these materials in hydrogen peroxide production.[88]

Upgrading the LIB waste sample using the second strategy – direct resynthesis of cathode materials

The second upgrading strategy is intended to form Co as the initial form of $LiCoO_2$ used in the fresh cathode of LIBs. Four samples went through this second strategy, all of them subjected to leaching and a final heat treatment step with temperatures of 550 °C (Res_Cath_550), 650 °C (Res_Cath_650), 750 °C (Res_Cath_750) and 850 °C (Res_Cath_850). These four samples were mixed with KJB (50 : 50 ratio) and they were tested electrochemically towards the ORR (Fig. 7), HER (Fig. 8a) and OER (Fig. 8b).

Oxygen reduction reaction electrocatalysis for samples series Res_Cath_*X*. E_{on} for these electrocatalysts was evaluated and ranged between 860 mV *vs.* RHE (Res_Cath_650) and 865 mV *vs.* RHE (Res_Cath_850). No clear relationship between this parameter (E_{on}) and the temperature treatment was detected. $E_{1/2}$ of these electrocatalysts ranged from 700 mV *vs.* RHE (Res_Cath_850) to 746 mV *vs.* RHE (Res_Cath_750). The limiting current density ranged between *ca.* 2.0 mA cm^{-2} and 3.8 mA cm^{-2} (Fig. 7a). Also in this case, the values measured were lower compared to the theoretical value, indicating an incomplete four-electron reaction mechanism. For single atom Fe–N–C type electrocatalyst, the ORR current density around 6 mA cm^{-2} is known owing to its higher ORR activity and particularly selectivity for direct 4-electron oxygen electroreduction. However, for Co, relatively inferior interaction with oxygen is known due to slightly less favourable electronic structure compared to Fe, which comes out as a preference for bielectronic or 2 × 2 stepwise ORR activity.[89] Even carbon-supported Co electrocatalysts in the typical configuration of Co–N–C have previously shown low limiting current densities under similar conditions.[90,91] The ring current densities were measured and reported in Fig. 7b and the peroxide produced was reported in Fig. 7c. In general, for this set of samples, the peroxide produced increased with the overpotentials, stabilizing at high overpotentials. This recorded trend was different from the previous set of electrocatalysts, where peroxide was reduced at higher overpotentials (Fig. 7c). Overall, the samples acquired during this stage presented lower peroxide yield, where the samples Res_Cath_850 and Res_Cath_750 produced peroxide less than 20%. Fig. 7d reports the number of electrons exchanged, which in this case decreased with increased overpotentials. The number of electrons varied from 3.6–3.8 at 600 mV *vs.* RHE to *ca.* 3.3–3.7 at 0 mV *vs.* RHE. These values are slightly higher with respect to the previous set of electrocatalysts (Metal_Pre_*X*). For comparison, the ORR activity of Pt/C, from our previous study,[92] is presented in Fig. S4. No doubt the activity profile in terms of E_{on} and $E_{1/2}$ is inferior compared to Pt/C, the peroxide yield remains comparable.

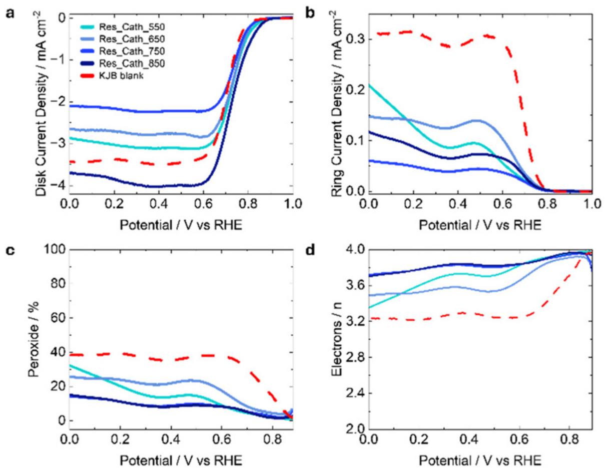

Fig. 7 Oxygen reduction reaction (ORR) performance of the samples of the Res_Cath_*X* series supported over 50% KJB. (a) Disk current density, (b) ring current density, (c) peroxide and (d) number of electrons exchanged.

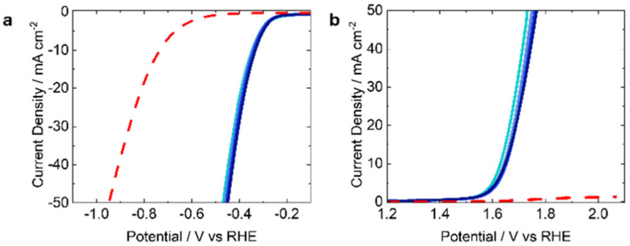

Fig. 8 (a) HER electrocatalytic activity and (b) OER electrocatalytic activity of the samples of the Res_Cath_*X* series supported over 50% KJB.

Hydrogen evolution reaction and oxygen evolution reaction results for samples series Res_Cath_*X*. LSVs related to HER, considering Res_Cath_*X* series (*X* = 550 °C, 650 °C, 750 °C and 850 °C) are reported in Fig. 8a, while LSVs done for measuring OER electrocatalytic activity of the same set of electrocatalysts are reported in Fig. 7b. HER overpotentials of this set of electrocatalysts are much lower compared to those recorded from the other set of electrocatalysts (Fig. 5a). HER overpotentials varied between 330 mV (Res_Cath_850) and 350 mV (Res_Cath_550) (Fig. 8a). A slight relationship between overpotentials and temperature treatment can be detected, with overpotentials slightly decreasing with increased temperature. Moreover, the sample Res_Cath_850 exhibited the least Tafel slope of 87.9 mV dec^{-1} as shown in Fig. S7a. These results were, in turn, comparable with the previous electrocatalytic activity reported by our research group.[63,70] Considering OER, the overpotentials ranged between 403 mV (Res_Cath_550) and 418 mV (Res_Cath_850) (Fig. 8b). These overpotential values are generally high, since commonly overpotentials below 300 mV are desired. Among the PGM-free electrocatalysts for OER, NiFe oxides can be considered state of the art electrocatalysts. Therefore, for comparison we have included the OER activity of the NiFe oxide from our previous study (with over potential *ca.* 291 mV) in SI as Fig. S5b.[65] While the activity is lower than that of state-of-the-art electrocatalysts, the value of waste-derived electrocatalysts should not be underestimated. Future research efforts can focus on reducing overpotentials and enhancing the performance of spent battery-derived electrocatalysts. Anyways, interestingly, the sample Res_Cath_550 demonstrated the lowest Tafel slope of 89.8 mV dec^{-1} while the other counterparts showed Tafel slopes between 105.5 and 107.7 mV dec^{-1} as shown in Fig. S7b. Besides, the samples were mixed with carbon, and the latter undergoes corrosion when operating at high potentials. However, to the best of our knowledge, no trials of these materials recovered from waste were tested for the OER in alkaline media, giving room for further improvement, especially when mixed with other transition metals in a desired ratio and morphological configuration.

Interestingly, compared to the samples obtained pursuing the first strategy, the ORR electrocatalytic activity is much improved, both in terms of E_{on} and $E_{1/2}$ but also as lower peroxide produced during ORR. In fact, at higher overpotentials, peroxide produced is roughly 15% with numbers of electrons exchanged above 3.7. Interestingly, also the HER and OER values are much improved, probably thanks to the different oxidation state of the Co within the mixture. The results are still a bit far from state of the art PGM-free electrocatalysts for OER and HER, however these results are quite promising and deserve further investigation.

Comparison with literature

Recovery of cobalt from the spent LIBs is one of the key focuses on contemporary research and development efforts in the paradigm of energy conversion and storage. As discussed, the reapplication of recovered cobalt into the batteries could lead to a complex route; however, its valorization and utilization in parallel energy technologies could open up new avenues in the pursuit of sustainability. In this regard, following two different strategies, waste cobalt was upgraded to serve as electrocatalysts in diverse electrochemical reactions. To begin with, cobalt-based electrocatalysts were derived from the spent batteries analyzed first for ORR in fuel cells, where the sample 'Res_Cath_850' exhibited an E_{on} of 885 mV *vs.* RHE, along with the least production of peroxide, with electron transfer number always remaining above 3.7 in 0.1 M KOH (pH 13). Res_Cath_850 sample also outperformed the other counterparts in HER and OER activities, giving the corresponding overpotentials of 330 and 418 mV *vs.* RHE, respectively, in 1.0 M KOH (pH 14). With the same aim, recently, Wang *et al.* recycled the spent LIBs and produced cobalt nitride nanoflowers that realized an ORR E_{on} of 938 mV in a nearly 4-electron ORR route during RRDE measurements in 1.0 M KOH.[93] The same study demonstrated the OER and HER potentials of 1.512 V *vs.* RHE and −188 mV *vs.* RHE for the cobalt nitride nanoflowers. In our previous report, we witnessed the 277 mV HER (1.0 M KOH) overpotential of the spent lithium cobalt oxide-based cathode, while the sample leached with deep eutectic solvent followed by a heat treatment ensured the ORR E_{on} of 850 mV *vs.* RHE with peroxide yield below 20% in 0.1 M KOH.[63] Moreover, Ruan *et al.* recycled discarded graphite from the anode of spent LIBs and used it to produce ORR electrocatalysts with Fe and N doping, which exhibited ORR activity with E_{on} of 0.91 V *vs.* RHE and excellent 4-electron ORR selectivity in 0.1 M KOH.[94] With similar aim, Liivand and coworkers attempted to produce electroatalyst from the spent batteries graphite in the post-metallurgical waste residue with *in situ* doped by the impurity Co that delivered efficient ORR activity in 0.1 M KOH with $E_{1/2}$ as high as 0.849 V.[95] In research reported by Arif *et al.*, lithium cobaltate was recovered from spent LIBs by treating the waste with citric acid, followed by a heat treatment and the obtained material displayed the OER overpotential of 550 mV *vs.* RHE.[96] Moreover, the impact of thermal treatments on the electrocatalytic activities of LIB-derived materials has also been analyze.[97,98] The performance comparison of the sample Res_Cath_850 with the recently reported LIB-derived electrocatalysts is shown in Table S3 for HER and OER, whereas Table S4 compares the ORR activities.

Conclusions

Cobalt is worldwide recognized as critical raw material (CRM) due to its central role in rechargeable batteries technology, where it is exploited in the cathode compartment. Cobalt is also emerging as an appealing alternative to platinum group metals (PGMs) based electrocatalysts in hydrogen production, combining good performance with lower cost than PGMs. Today, cobalt is one of the key elements that drives the development of industrial recycling of spent lithium-ion batteries (LIBs), as its recovery represents the main economic driving force in the implementation of recycling procedures. Recycling of spent-LIBs is performed at industrial level and allows for the recovery of Co in form of metal or oxides while new strategies are actively developed at research level for the direct resynthesis of new cathode materials from the spent-LIBs. With the aim to maximize and optimize the utilization of cobalt, in the present paper, we explore the possibility to produce electrocatalysts from cobalt oxides (representative products or byproducts of the industrial recycling routes of spent-LIBs) and from $LiCoO_2$ (representative of products or byproducts of new direct recycling procedures). This study confirms that the products derived from these two recycling strategies can be exploited as promising electrocatalysts for: (i) the oxygen reduction reaction and eventually hydrogen peroxide production by tailoring the synthesis toward higher faradaic efficiencies, (ii) the hydrogen evolution reaction and (iii) oxygen evolution reaction. The ultimate substitution of PGMs in fuel cells and electrolyzers is paramount and further integrations of transition metals coming from different sources will be extremely valuable within the core of circularity and hence open new research fields.

As a perspective, this approach can be extended to other relevant spent LIBs cathode, such as $Li(Ni/Mn/Co)O_2$ oxides (NMC) and $LiFePO_4$ (LFP) to further tune the electrocatalytic properties and valorise production scraps.

Author contributions

A. M. and J. F. have been involved in the black mass recovery, E. C. in the sample preparation and physico chemical characterization. L. C. J. and M. M. are responsible for the electrode preparation and electrochemical testing. E. B. is responsible for TEM and SEM analysis. A. G. M. is responsible for XPS analysis. C. F., C. S., M. M. have been in charge of project planning, data curation, writing.

Conflicts of interest

There are no conflicts to declare.

Data availability

All data presented in the present study are presented in the figures and tables of this paper.

Supplementary information (SI) is available. See DOI: https://doi.org/10.1039/d5nr05348j.

The data are available from the corresponding author upon reasonable request.

Acknowledgements

C. F., A. M. and J. F. acknowledge financial support from the Fondazione Cariplo through the grant "Cathode Recovery for lithium-ion battery recycling, COLIBRI", and the financial support from the project MUR-PRIN "Enhanced metals recovery by coordination chemistry from lithium batteries waste-ERCOLE" project code 2022JPT7YW. C. F. also acknowledges the financial support from the European Union's Horizon Europe research and innovation program under the Grant Agreement No. 101137745 (RENOVATE) and 101104022 (BATTERY 2030 CSA3) and Regione Lombardia (IT) in the context of the institutional agreement in the establishment of EcoCirc facilities for a "System integrator towards circular economy".

C. S. and M. M. would like to acknowledge the National recovery and resilience Plan (PNRR), Mission 2 "Green Revolution and Ecological Transition", Component 2 "Renewable Energy, Hydrogen, Network and Sustainable Mobility", Investment 3.5 "Hydrogen Research and Development", European Union – Next Generation EU – Italian Ministry of Environment and Energy Security (MASE), project AMBITION.

C. S. would like to acknowledge also the Cariplo Foundation, Call for Circular Economy through the project "Transformation of plastic waste in Electrocatalysts, Supported by exhausted gases recovery Layout" (TESLA).

L. C. J. would like to acknowledge the Consejería de Universidad, Investigación e Innovación of the Junta de Andalucía for the PAIDI 2020 Postdoctoral Grant, co-funded by the European Social Fund (ref. DOC 01168); the Ministerio de Ciencia, Innovación y Universidades for the José Castillejo 2022 Fellowship; and the University of Malaga for support through the B.1. Ayudas para proyectos dirigidos por jovenes investigadores (ref. B1-2021_03).

References

1 IEA, *Global EV Outlook 2024*, 2024.
2 Critical Mineral List in Korea – Policies, https://www.iea.org/policies/17943-critical-mineral-list-in-korea, (accessed 2 December 2025).
3 O. US EPA, Summary of Inflation Reduction Act provisions related to renewable energy, https://www.epa.gov/green-power-markets/summary-inflation-reduction-act-provisions-related-renewable-energy, (accessed 2 December 2025).
4 UK Government, *UK Critical Minerals Strategy*, 2025.
5 European Parliament, *Critical Raw Materials Act*, 2023.
6 European Commission, *Waste and recycling - Batteries*, 2025.
7 A. D. A. Bin Abu Sofian, S. R. Majid, K. Kang, J.-K. Kim and P. L. Show, *Prog. Mater. Sci.*, 2025, **153**, 101478.
8 F. Ahmad, A. Arif, M. I. Khan, S. Anjum, A. Shanableh, M. B. Taj and R. Luque, *J. Power Sources*, 2025, **648**, 237362.
9 J. Li, S. Nazari, X. Ma, N. Wei and Y. He, *Next Mater.*, 2025, **8**, 100641.
10 G. Harper, R. Sommerville, E. Kendrick, L. Driscoll, P. Slater, R. Stolkin, A. Walton, P. Christensen, O. Heidrich, S. Lambert, A. Abbott, K. Ryder, L. Gaines and P. Anderson, *Nature*, 2019, **575**, 75–86.
11 E. Carena, D. Brambilla, M. Vergani, R. Morina, N. Pianta and C. Ferrara, *Energy Fuels*, 2024, **38**, 18044–18053.
12 H. Deng, B. Wang, J. Xu, G. Yang, Z. Shi, H. Zhu, W. He and G. Li, *Sep. Purif. Technol.*, 2025, **363**, 132234.
13 C. Lee, D. S. Arby, C. Kim, J. Lim, K. Kwon and E. Chung, *Hydrometallurgy*, 2025, **235**, 106494.
14 M. Jafari, S. Z. Shafaie, H. Abdollahi and A. Entezari-Zarandi, *J. Environ. Chem. Eng.*, 2022, **10**, 109014.

15 Y. Hua, Y. Sun, F. Yan, S. Wang, Z. Xu, B. Zhao and Z. Zhang, *Chem. Eng. J.*, 2022, **436**, 133200.

16 R. Morina, E. Carena, N. Pianta, E. Perona, I. Ostroman, P. Mustarelli and C. Ferrara, *J. Environ. Manage.*, 2024, **370**, 122827.

17 C. Ma, M. Svärd and K. Forsberg, *Resour., Conserv. Recycl.*, 2022, **186**, 106579.

18 Q. Lu, L. Chen, X. Li, Y. Chao, J. Sun, H. Ji and W. Zhu, *ACS Sustainable Chem. Eng.*, 2021, **9**, 13851–13861.

19 S. Natarajan and S. Noda, *Mater. Sci. Eng.*, 2025, **164**, 100976.

20 B. Lu, R. Du, G. Wang, Y. Wang, S. Dong, D. Zhou, S. Wang and C. Li, *Environ. Res.*, 2022, **212**, 113286.

21 Y. Chen, Y. Kang, Y. Zhao, L. Wang, J. Liu, Y. Li, Z. Liang, X. He, X. Li, N. Tavajohi and B. Li, *J. Energy Chem.*, 2021, **59**, 83–99.

22 Battery plant scrap rates can hit 90% at ramp up, but the situation is improving, https://www.autoweek.com/news/a46628833/early-production-battery-plant-scrap-rates/, (accessed 2 December 2025).

23 C. Santoro, A. Lavacchi, P. Mustarelli, V. D. Noto, L. Elbaz, D. R. Dekel and F. Jaouen, *ChemSusChem*, 2022, **15**, e202200027.

24 H. F. Araújo, J. A. Gómez and D. M. F. Santos, *Catalysts*, 2024, **14**, 845.

25 S. Zhang, X. He, Y. Ding, Z. Shi and B. Wu, *Renewable Sustainable Energy Rev.*, 2024, **204**, 114821.

26 P. Wang, C. Wang, J. Li, K. Hubacek, L. Sun, F. Yang, K. Feng and W.-Q. Chen, *PNAS Nexus*, 2024, **3**, 172.

27 A. E. Hughes, N. Haque, S. A. Northey and S. Giddey, *Resources*, 2021, **10**, 93.

28 R. Kleijn and E. van der Voet, *Renewable Sustainable Energy Rev.*, 2010, **14**, 2784–2795.

29 T. C. Dzogbewu and D. J. de Beer, *Manuf. Rev.*, 2024, **11**, 16.

30 T. Uekert, H. M. Wikoff and A. Badgett, *Adv. Sustainable Syst.*, 2024, **8**, 2300449.

31 S. Aslam, S. Rani, K. Lal, M. Fatima, T. Hardwick, B. Shirinfar and N. Ahmed, *Green Chem.*, 2023, **25**, 9543–9573.

32 T. Smolinka, E. T. Ojong, J. Garche, Chapter 8 - Hydrogen Production from Renewable Energies—Electrolyzer Technologies, in *Electrochemical Energy Storage for Renewable Sources and Grid Balancing*, ed. P. T. Moseley and J. Garche, Elsevier, 2015, pp. 103–128.

33 T. Jamal, G. M. Shafiullah, F. Dawood, A. Kaur, M. T. Arif, R. Pugazhendhi, R. M. Elavarasan and S. F. Ahmed, *Energy Rep.*, 2023, **10**, 2103–2127.

34 B. C. Tashie-Lewis and S. G. Nnabuife, *Chem. Eng. J. Adv.*, 2021, **8**, 100172.

35 J. C. Koj, P. Zapp, C. Wieland, K. Görner and W. Kuckshinrichs, *J. Ind. Ecol.*, 2025, **29**, 145–158.

36 Y. Wang, Y. Pang, H. Xu, A. Martinez and K. S. Chen, *Energy Environ. Sci.*, 2022, **15**, 2288–2328.

37 K. Ayers, N. Danilovic, K. Harrison and H. Xu, *Electrochem. Soc. Interface*, 2021, **30**, 67.

38 S. Mo, L. Du, Z. Huang, J. Chen, Y. Zhou, P. Wu, L. Meng, N. Wang, L. Xing, M. Zhao, Y. Yang, J. Tang, Y. Zou and S. Ye, *Electrochem. Energy Rev.*, 2023, **6**, 28.

39 Y. Wang, D. F. Ruiz Diaz, K. S. Chen, Z. Wang and X. C. Adroher, *Mater. Today*, 2020, **32**, 178–203.

40 C. Gerling, M. Hanauer, U. Berner and K. A. Friedrich, *J. Electrochem. Soc.*, 2022, **169**, 014503.

41 Ni Suo, L. Cao, X. Qin and Z. Shao, *Chin. Phys. B*, 2022, **31**, 128108.

42 K. J. Ferner and S. Litster, *ACS Appl. Energy Mater.*, 2024, **7**, 8124–8135.

43 C. Wang and L. Feng, *Energy Adv.*, 2024, **3**, 14–29.

44 Y. Du, J. Liu, J. Chen, S. Wang, Y. Tang, A.-L. Wang, G. Fu and X. F. Lu, *Adv. Energy Mater.*, 2025, **15**, 2404113.

45 M. Khalili, H. M. A. Harameen, B. Choi, M. Bae, H. Lee, S.-K. Kim and C. Lee, *ACS Appl. Energy Mater.*, 2025, **8**, 8641–8655.

46 T. Uekert, H. M. Wikoff and A. Badgett, *Adv. Sustainable Syst.*, 2024, **8**, 2300449.

47 M. Chatenet, B. G. Pollet, D. R. Dekel, F. Dionigi and H. Schäfer, *Chem. Soc. Rev.*, 2022, **11**, 4583–4762.

48 M. Muhyuddin, C. Santoro, L. Osmieri and P. Atanassov, *Chem. Rev.*, 2025, **125**, 6906–6976.

49 H. A. Miller, K. Bouzek, J. Hnat, S. Loos, C. I. Bernäcker, T. Weißgärber, L. Röntzsch and J. Meier-Haack, *Sustainable Energy Fuels*, 2020, **4**, 2114–2133.

50 N. A. A. Qasem and G. A. Q. Abdulrahman, *Int. J. Energy Res.*, 2024, **2024**, 7271748.

51 W. Zeng, B. Guan, Z. Zhuang, J. Chen, L. Zhu, Z. Ma, X. Hu, C. Zhu, S. Zhao, K. Shu, H. Dang, T. Zhu and Z. Huang, *Int. J. Hydrogen Energy*, 2025, **102**, 222–246.

52 J. R. Varcoe, P. Atanassov, D. R. Dekel and L. Zhuang, *Energy Environ. Sci.*, 2014, **10**, 3135–3191.

53 S. Gottesfeld, D. R. Dekel, M. Page, C. Bae, Y. Yan, P. Zelenay and Y. S. Kim, *J. Power Sources*, 2018, **375**, 170–184.

54 C. Xiao, H. Huang, Z. Zhang, Y. Jiang, G. Wang, H. Liu, Y. Liu, L. Xing and L. Zeng, *J. Power Sources*, 2024, **606**, 234509.

55 H. C. Honig, S. Mostoni, Y. Presman, R. Z. Snitkoff-Sol, P. Valagussa, M. D'Arienzo, R. Scotti, C. Santoro, M. Muhyuddin and L. Elbaz, *Nanoscale*, 2024, **16**, 11174–11186.

56 S. Mostoni, L. Mirizzi, A. Frigerio, G. Zuccante, C. Ferrara, M. Muhyuddin, M. D'Arienzo, S. F. Orsini, R. Scotti, A. Cosenza, P. Atanassov and C. Santoro, *ChemSusChem*, 2025, **18**, e202401185.

57 S. A. Mirshokraee, M. Muhyuddin, J. Orsilli, E. Berretti, A. Lavacchi, C. L. Vecchio, V. Baglio, R. Viscardi, A. Zaffora, F. D. Franco, M. Santamaria, L. Olivi, S. Pollastri and C. Santoro, *Nanoscale*, 2024, **16**, 6531–6547.

58 A. Serov, M. J. Workman, K. Artyushkova, P. Atanassov, G. McCool, S. McKinney, H. Romero, B. Halevi and T. Stephenson, *J. Power Sources*, 2016, **327**, 557–564.

59 A. Serov, M. H. Robson, M. Smolnik and P. Atanassov, *Electrochim. Acta*, 2013, **109**, 433–439.

60 L. Wang, J. J. Brink and J. R. Varcoe, *Chem. Commun.*, 2017, **53**, 11771–11773.

61 A. Raut, H. Fang, Y.-C. Lin, S. Fu, M. F. Rahman, D. Sprouster, L. Wang, Y. Fang, Y. Yin, D. Bhardwaj, R. Isseroff, T.-D. Li, M. Cuiffo, J. C. Douglin, J. Lilloja,

K. Tammeveski, D. R. Dekel and M. Rafailovich, *Carbon Trends*, 2025, **19**, 100451.

62 A. A. Jeffery, S. S. Chougule, M. Sharma, Y. Kim, K. Ko, J. Min, J. Heo, H.-K. Lim and N. Jung, *Nanoscale*, 2025, **17**, 19377–19389.

63 S. A. Mirshokraee, M. Muhyuddin, R. Morina, L. Poggini, E. Berretti, M. Bellini, A. Lavacchi, C. Ferrara and C. Santoro, *J. Power Sources*, 2023, **557**, 232571.

64 F. Malaj, D. Lentini, A. Tampucci, L. Brogi, E. Berretti, M. Muhyuddin, G. Baiardi, S. Forti, A. Rossi, C. Coletti, O. Tarallo, F. Ruffo and C. Santoro, *Electrochim. Acta*, 2025, **536**, 146805.

65 L. Mirizzi, M. Muhyuddin, C. L. Vecchio, E. Mosca, V. Baglio, I. Gatto, E. Berretti, A. Lavacchi, V. C. A. Ficca, R. Viscardi, R. Nisticò and C. Santoro, *Ind. Chem. Mater.*, 2025, **3**, 485–497.

66 W. Moschkowitsch, B. Samanta, N. Zion, H. C. Honig, D. A. Cullen, M. C. Toroker and L. Elbaz, *Nanoscale*, 2022, **14**, 18033–18040.

67 K. Wang, Y. Xu, V. Daneshvariesfahlan, M. Rafique, Q. Fu, H. Wei, Y. Zhang, J. Zhang, B. Zhang and B. Song, *Nanoscale*, 2025, **17**, 6287–6307.

68 Y. Zeng, X. Wang, Y. Hu, W. Qi, Z. Wang, M. Xiao, C. Liu, W. Xing and J. Zhu, *Carbon Neutralization*, 2024, **3**, 710–736.

69 A. A. Feidenhans'l, Y. N. Regmi, C. Wei, D. Xia, J. Kibsgaard and L. A. King, *Chem. Rev.*, 2024, **124**, 5617–5667.

70 L. Mirizzi, E. Carena, C. Santoro, V. C. A. Ficca, E. Placidi, E. Berretti, A. Lavacchi, C. Ferrara and M. Muhyuddin, *Mater. Renewable Sustainable Energy*, 2025, **14**, 37.

71 C. Ferrara and R. Morina, Procedimento per il riciclo di batterie al litio, Patent number 102023000022644, 2023, https://www.uibm.gov.it/bancadati, (accessed 27 April 2025).

72 J. H. Scofield, *J. Electron Spectrosc. Relat. Phenom.*, 1976, **8**, 129–137.

73 M. C. Biesinger, B. P. Payne, A. P. Grosvenor, L. W. M. Lau, A. R. Gerson and R. S. C. Smart, *Appl. Surf. Sci.*, 2011, **257**, 2717–2730.

74 T. J. Chuang, C. R. Brundle and D. W. Rice, *Surf. Sci.*, 1976, **59**, 413–429.

75 R. Dedryvère, S. Laruelle, S. Grugeon, P. Poizot, D. Gonbeau and J.-M. Tarascon, *Chem. Mater.*, 2004, **16**, 1056–1061.

76 G. A. Carson, M. H. Nassir and M. A. Langell, *J. Vac. Sci. Technol., A*, 1996, **14**, 1637–1642.

77 V. R. Galakhov, V. V. Karelina, D. G. Kellerman, V. S. Gorshkov, N. A. Ovechkina and M. Neumann, *Phys. Solid State*, 2002, **44**, 266–273.

78 J. van Elp, J. L. Wieland, H. Eskes, P. Kuiper, G. A. Sawatzky, F. M. F. de Groot and T. S. Turner, *Phys. Rev. B: Condens. Matter Mater. Phys.*, 1991, **44**, 6090–6103.

79 L. Dahéron, R. Dedryvère, H. Martinez, M. Ménétrier, C. Denage, C. Delmas and D. Gonbeau, *Chem. Mater.*, 2008, **20**, 583–590.

80 D. Ensling, G. Cherkashinin, S. Schmid, S. Bhuvaneswari, A. Thissen and W. Jaegermann, *Chem. Mater.*, 2014, **26**, 3948–3956.

81 A. Thissen, D. Ensling, F. J. Fernández Madrigal, W. Jaegermann, R. Alcántara, P. Lavela and J. L. Tirado, *Chem. Mater.*, 2005, **17**, 5202–5208.

82 P. G. Schiavi, A. G. Marrani, O. Russina, L. D'Annibale, F. Amato, F. Pagnanelli and P. Altimari, *J. Energy Chem.*, 2024, **88**, 144–153.

83 D. Giacco, T. Skála, S. Brutti and A. G. Marrani, *ACS Appl. Nano Mater.*, 2023, **6**, 10178–10190.

84 A. Bergmann, E. Martinez-Moreno, D. Teschner, P. Chernev, M. Gliech, J. F. de Araújo, T. Reier, H. Dau and P. Strasser, *Nat. Commun.*, 2015, **6**, 8625.

85 D. Hein, G. Wartner, A. Bergmann, M. Bernal, B. Roldan Cuenya and R. Seidel, *ACS Nano*, 2020, **14**, 15450–15457.

86 J. Shi, M. Fan, J. Qiao and Y. Liu, *Chem. Lett.*, 2014, **43**, 1484–1486.

87 K. Gong, F. Du, Z. Xia, M. Durstock and L. Dai, *Science*, 2009, **323**, 760–764.

88 Y. Zhou, G. Chen and J. Zhang, *J. Mater. Chem. A*, 2020, **8**, 20849–20869.

89 K. Singh, F. Razmjooei and J.-S. Yu, *J. Mater. Chem. A*, 2017, **5**, 20095–20119.

90 M. Muhyuddin, E. Berretti, J. Orsilli, L. Mirizzi, R. Landone, F. D'acapito, A. Cosenza, S. Faina, M. Arienzo, I. Nadeem, M. Kalin, P. Atanassov, C. Santoro and A. Lavacchi, *ACS Catal.*, 2026, **16**, 2065–2082.

91 E. Jung, H. Shin, B.-H. Lee, V. Efremov, S. Lee, H. S. Lee, J. Kim, W. Hooch Antink, S. Park, K.-S. Lee, S.-P. Cho, J. S. Yoo, Y.-E. Sung and T. Hyeon, *Nat. Mater.*, 2020, **19**, 436–442.

92 S. A. Mirshokraee, M. Muhyuddin, R. Lorenzi, G. Tseberlidis, C. L. Vecchio, V. Baglio, E. Berretti, A. Lavacchi and C. Santoro, *SusMat*, 2023, **3**, 248–262.

93 Z. Wang, M. Li, B. Fu, W. Cao and X. Bo, *J. Colloid Interface Sci.*, 2024, **662**, 218–230.

94 D. Ruan, K. Zou, K. Du, F. Wang, L. Wu, Z. Zhang, X. Wu and G. Hu, *ChemCatChem*, 2021, **13**, 2025–2033.

95 K. Liivand, J. Sainio, B. P. Wilson, I. Kruusenberg and M. Lundström, *Appl. Catal., B*, 2023, **332**, 122767.

96 A. Arif, M. Xu, J. Rashid, C. S. Saraj, W. Li, B. Akram and B. Hu, *Nanomaterials*, 2021, **11**, 3343.

97 V. C. B. Pegoretti, P. V. M. Dixini, L. Magnago, A. K. S. Rocha, M. F. F. Lelis and M. B. J. G. Freitas, *Mater. Res. Bull.*, 2019, **110**, 97–101.

98 J. Wei, S. Zhao, L. Ji, T. Zhou, Y. Miao, K. Scott, D. Li, J. Yang and X. Wu, *Resour., Conserv. Recycl.*, 2018, **129**, 135–142.